Nuclear Science and Techniques (2024) 35:212
https://doi.org/10.1007/s41365-024-01586-z

Reaction dynamics of proton-rich nuclei at energies around the Coulomb barrier: the cases of ^{7}Be, ^{8}B, and ^{17}F

Tian-Peng Luo[1] · Lei Yang[1] · Cheng-Jian Lin[1] · Nan-Ru Ma[1] · Pei-Wei Wen[1] · Hui-Ming Jia[1] · Feng Yang[1]

Received: 15 July 2024 / Revised: 19 August 2024 / Accepted: 9 September 2024

Abstract
The exploration of reaction dynamics, particularly the breakup and fusion mechanisms of proton drip-line nuclei at energies around the Coulomb barrier, is crucial in the field of nuclear physics. This study reviews experimental investigations on the reactions induced by proton-rich nuclei, ^{7}Be, ^{8}B, and ^{17}F, including elastic scattering and direct and fusion reactions at the near-barrier energies. In particular, we briefly introduce complete kinematic measurements of ^{8}B+^{120}Sn and ^{17}F+^{58}Ni at the energies of interest. Distinct reaction dynamics are observed for proton-rich nuclei compared with neutron-rich nuclei.

Keywords Proton-rich nuclei · Energies around the Coulomb barrier · Elastic scattering · Breakup reactions · Fusion reactions

1 Introduction

With improvements in the quality of radioactive beams and upgrades in detection techniques, the study of the nuclear structure and reaction mechanisms of radioactive nuclei have become popular in the field of nuclear physics [1–5]. For tightly bound nuclear systems, only a few reaction channels such as inelastic scattering, transfer, and fusion reactions are typically open in the Coulomb barrier energy region. However, the reaction mechanism for weakly bound nuclear systems is complex. Owing to their low separation energies, the projectile nuclei can easily breakup during the collision. At energies near the Coulomb barrier, the breakup reaction has strong coupling effects on other processes, such as elastic scattering and fusion reactions, thereby affecting the reaction dynamics of the entire system [1, 6, 7].

Recently, numerous experiments and theoretical studies have been conducted on weakly bound neutron-rich nuclear systems at energies near the Coulomb barrier, as reviewed in Refs. [6–8]. For elastic scattering, measurements involving neutron-halo nuclei such as ^{6}He [9, 10], ^{11}Li [11], and ^{11}Be [12, 13] show considerable suppression of the Coulomb rainbow peak. This can be properly described by continuum discretized coupled-channels (CDCC) calculations, indicating strong coupling effects to the continuum states. Owing to the difficulties in detecting neutrons with high efficiency for direct reactions, few attempts have been made to measure the alpha and neutron coincidence for the ^{6}He+^{209}Bi system [14]. The results established that the neutron-transfer reaction is the dominant direct reaction rather than breakup. The dynamics of fusion reactions induced by weakly bound nuclei are an interesting topic: extended nuclear densities with tails induce lower fusion barriers, resulting in an enhanced fusion cross-section; however, the emergence of breakup channels may attenuate the incident current, which may hinder the complete fusion of the cross-section [1, 6]. Based on the large amount of data from neutron-halo systems [1], the total fusion cross-section is suppressed owing to breakup effects at energies above the Coulomb barrier and enhancement at sub-barrier energies.

In a proton-rich nuclear system, an additional Coulomb interaction exists between the valence proton and core as

Dedicated to Professor Wenqing Shen in honor of his 80th birthday.

This work was supported by the National Key R&D Program of China (No. 2022YFA1602302), the National Natural Science Foundation of China (Nos. U2167204, 12175314, and 12235020), and the Continuous-Support Basic Scientific Research Project.

✉ Lei Yang
yang_lei@ciae.ac.cn

✉ Cheng-Jian Lin
cjlin@ciae.ac.cn

[1] China Institute of Atomic Energy, Beijing 102413, China

Published online: 23 November 2024

well as between the valence proton and target. The dynamic Coulomb polarization effect [15, 16] can suppress both proton-transfer and breakup processes [17]. Therefore, compared to the neutron-rich systems, distinct reaction dynamics are expected in proton-rich nuclear systems. However, experimental data pertaining to proton-rich nuclei at energies around the Coulomb barrier are scarce owing to beam-intensity constraints [8]. With improvements in the detection efficiency of detector arrays, several delicate experiments have been conducted to study the reaction dynamics of proton-rich nuclear systems. Considering the feasibility of measurements, research endeavors have predominantly centered on investigating ^{7}Be, ^{8}B, and ^{17}F. Therefore, the available data should be reviewed to summarize what can be learn from them. In this study, we first briefly review the current results for ^{7}Be, ^{8}B, and ^{17}F at the energies of interest. Description and discussion of the complete kinematics measurements of ^{8}B and ^{17}F are provided. Finally, we present our conclusions and outlook for this topic.

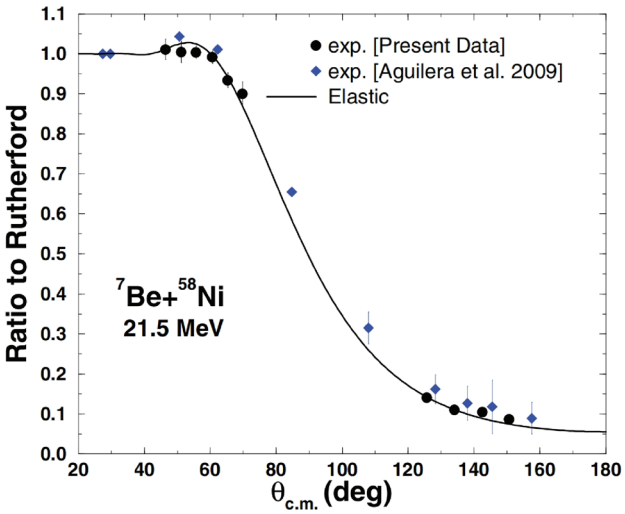

Fig. 1 Quasi-elastic scattering angular distribution of ^{7}Be+^{58}Ni at 21.5 MeV. The circles and diamonds represent experimental data taken from Refs. [18, 19]. The solid curve denotes the optical-model calculation result. The figure is sourced from Ref. [18]

2 Experimental results of ^{7}Be

^{7}Be is a proton-drip-line nucleus characterized by a small alpha-separation energy of 1.586 MeV. Hence, it can easily break up into ^{3}He and ^{4}He when interacting with a target. ^{7}Be is a radioactive nucleus with a half-life of 53.2 d. To date, several studies have reported elastic-scattering data for ^{7}Be at energies around the Coulomb barrier [8]. However, experimental data on the breakup and fusion of this isotope are scarce.

2.1 Elastic scattering of ^{7}Be

The elastic-scattering data for ^{7}Be on light targets of ^{7}Li, ^{10}B, ^{12}C, ^{14}N, and ^{27}Al were reviewed in Refs. [7, 8]. Data on medium- and heavy-target systems are emphasized here.

2.1.1 ^{7}Be+^{58}Ni

The elastic scattering of ^{7}Be+^{58}Ni at an energy of 21.5 MeV has been measured by Mazzocco et al. [18]. The resulting angular distribution is presented in Fig. 1 with the data obtained by Aguilera et al. [19], which are represented by diamond symbols. Notably, the first excited state of ^{7}Be ($E_{ex.} = 0.43$ MeV) cannot be identified; thus, these data must be considered as quasi-elastic scattering. Optical model calculation utilizing the potential parameters of ^{7}Li values from Cook et al. [20] is presented in Fig. 1 using a solid curve. This model is devoid of free parameters and presents an appropriate description of the experimental data. Additionally, a CDCC calculation was performed using a ^{3}He–^{4}He two-body structure for ^{7}Be. In the CDCC calculation, the potential parameters for the ^{4}He-target interaction were derived by fitting the elastic-scattering data of ^{4}He and ^{58}Ni at 12 MeV [21]. The parameters for the ^{3}He–^{58}Ni interaction were derived from Fick et al. [22]. The interaction between ^{3}He and ^{4}He were characterized using the parameters reported by Buck et al. [23]. Similar to the optical model, the CDCC calculation provided a satisfactory representation of the data, indicating minor coupling effects to the continuum states of ^{7}Be.

2.1.2 ^{7}Be+^{120}Sn

We experimentally investigated ^{7}Be+^{120}Sn using the Radioactive Ion Beam Line in Lanzhou (RIBLL1), a facility at the Institute of Modern Physics, Chinese Academy of Sciences [24, 25]. The secondary beam of ^{7}Be, which was purified by RIBLL1, was sent to a self-supporting isotopically enriched ^{120}Sn target with a thickness of 2.78 mg/cm^{2}. The beam was characterized by an energy of 48.05 ± 0.9 MeV in the middle of the secondary target ^{120}Sn. Throughout the experiment, the beam intensity was maintained at a typical rate of 1×10^{5} particles per second (pps), with a purity of approximately 90%.

The angular distribution of the elastic scattering of ^{7}Be+^{120}Sn is shown in Fig. 2. Notably, the total energy resolution of our measurements was insufficient for the distinct differentiation of the first excited states of ^{7}Be.

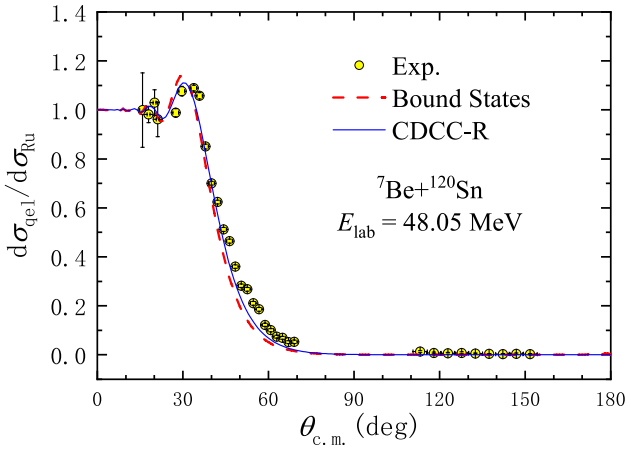

Fig. 2 Elastic-scattering angular distribution of ^{7}Be+^{120}Sn at 48.05 MeV. The solid and dashed curves represent the CDCC-R calculations with and without the couplings to the unbound states

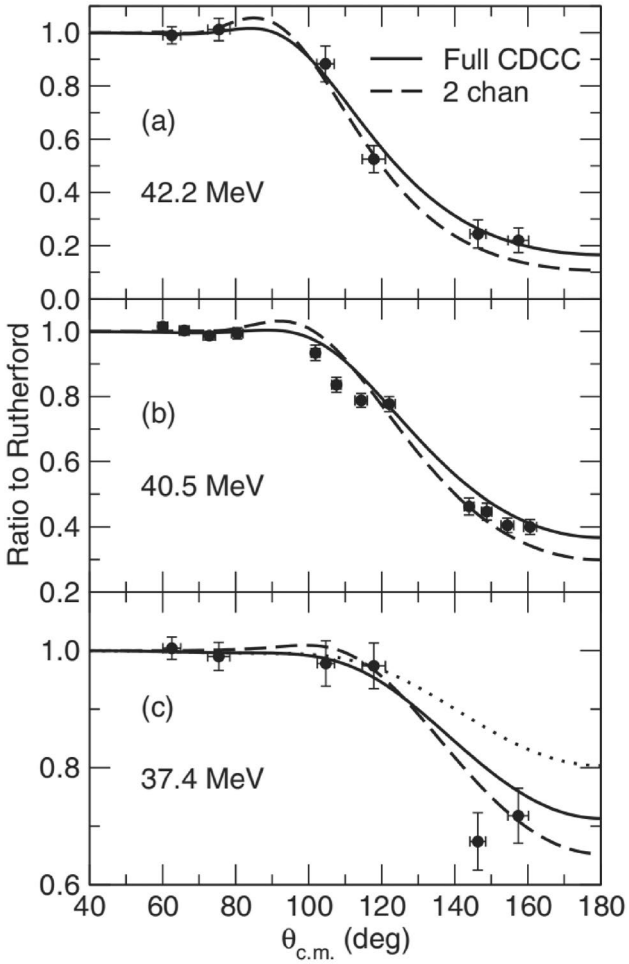

Fig. 3 Quasi-elastic-scattering angular distributions of ^{7}Be+^{208}Pb at **a** 42.2, **b** 40.5, and **c** 37.4 MeV. The solid and dashed curves represent the full CDCC and two-channel calculation results, respectively. The dotted curve in **c** denotes the CDCC calculation for 37.4 MeV with the same ^{3}He+^{208}Pb potential parameters as those at 42.2 and 40.5 MeV. The figures are sourced from Ref. [31]

Consequently, the scattering data must be interpreted as quasi-elastic scattering.

We employed a novel framework known as CDCC with Regularization (CDCC-R), as outlined by Chen et al. [26], to analyze the scattering data. This CDCC-R approach leverages the highly efficient regularized Lagrange–Laguerre Mesh (RLLM) technique [27] to construct pseudo-states. A significant innovation within this methodology is the integration of RLLM with the modified Numerov algorithm [28], which not only accelerates the computational process, but also provides the convenient handling of closed channels within the CDCC-R framework. In the CDCC-R calculations, ^{7}Be is described using a ^{3}H+^{4}He two-body model. The nuclear interaction between these two clusters is encapsulated in a Gaussian form, which is applied to both the central and spin-orbit coupling terms. The CDCC-R method also encompasses the bound $1/2^{-}$ first excited state of ^{7}Be, thereby enabling a comprehensive analysis of the system. The framework adeptly handles continuous spaces, including two l=3 resonances ($7/2^{-}$ and $5/2^{-}$ at excitation energies of $E_{ex.}$ = 4.57 and 6.73 MeV with widths of Γ of 0.18 and 1.2 MeV, respectively). In addition, a nonresonant continuum extending from $l = 0$ to $l = 4$ was incorporated into the calculations. The discretization of the momentum space was set uniformly with bin intervals Δk of 0.1 fm^{-1}. To ensure the accuracy of the calculations, the Legendre-polynomial expansion was extended to the eighth order. The optical potentials of the interactions of ^{4}He and ^{3}He with ^{120}Sn were derived from Refs. [29, 30].

The CDCC-R results are presented in Fig. 2, where the solid and dashed curves correspond to the results with and without the couplings to the continuum states, respectively. A comparative analysis revealed that the influence of the continuum states of ^{7}Be on elastic scattering is relatively minor. In addition, the calculated contribution of the elastic breakup cross-section of ^{7}Be to the total reaction cross-section, was merely 2%, revealing the minimal role played by this process in the total reaction process. Furthermore, an examination of the inelastic scattering channel leading to the excitation of the first excited state of ^{7}Be reveals a contribution that is effectively negligible.

2.1.3 ^{7}Be+^{208}Pb

The elastic scattering of ^{7}Be+^{208}Pb was measured by Mazzocco [31] at energies of 37.4, 40.5, and 42.2 MeV. The angular distributions derived from these measurements are shown in Fig. 3. Notably, these measurements yielded results similar to those obtained in previous studies, which are classified as quasi-elastic owing to the indistinguishability of

the excitation to the first excited state of ^{7}Be from elastic-scattering events.

The results of the CDCC calculations are shown in Fig. 3 using solid curves. For a comparative analysis, the dashed curves in the figure illustrate the results of the two-channel calculations, which account for the ground-state reorientation and coupling to the first excited state of ^{7}Be. CDCC calculations provide a proper description of quasi-elastic scattering data. Furthermore, the subtle discrepancies observed between the CDCC and two-channel calculations are indicative of the modest influence that the coupling to the continuum states of ^{7}Be exerts on elastic scattering.

Sensitivity analysis of the calculations for the choice of the ^{4}He+^{208}Pb interaction potential indicated a relatively low dependency. To reveal the importance of fine-tuning the ^{3}He+^{208}Pb optical potential, a comparative analysis of the quasi-elastic scattering derived from the CDCC calculation at 37.4 MeV is shown in Fig. 3c. This calculation utilizes the identical ^{3}He+^{208}Pb optical potential employed at the higher energies of 42.2 and 40.5 MeV. Notably, this approach results in a significant overestimation of the differential cross-section at backward angles, thereby highlighting the necessity of a potential adjustment to achieve congruence with the experimental data at a lower energy.

The total reaction and breakup cross-sections were derived using two-channel and CDCC calculations. The results revealed that the breakup cross-sections constitute a relatively modest proportion of the total reaction cross-section, typically on the order of 10%.

2.2 Breakup of ^{7}Be

To date, the measurements of direct reactions involving ^{7}Be are limited, and only a few inclusive measurements have been reported. Mazzocco et al. conducted an experiment using ^{7}Be and ^{58}Ni at an energy of 22 MeV [18]. However, owing to limitations in the detection efficiency, no coincidence between the breakup fragments of ^{3}He and ^{4}He was observed. The calculation of the CDCC yielded an elastic breakup cross-section for the ^{7}Be+^{58}Ni system of a mere 10.8 mb. This result reveals the relatively minor contribution of the breakup channel to the total reaction cross-section.

The ^{7}Be+^{12}C system was experimentally investigated at an incident energy of 34 MeV [32]. Few ^{3}He–^{4}He coincident events were observed, which is inadequate to set an upper limit for the breakup cross-section. Pronounced selectivity was observed for the ^{12}C (^{7}Be, ^{3}He) reaction, populating the α-cluster states in ^{16}O. Furthermore, the measured angular distributions of the emitted ^{3}He particles were predominantly forward-peaked. These two features suggested that the direct α-transfer mechanism is the predominant process responsible for the observed yield of ^{3}He particles, rather than the breakup process.

2.3 Fusion of ^{7}Be

The fusion reactions induced by ^{7}Be were measured using the targets of ^{27}Al [33], ^{58}Ni [34], and ^{238}U [35]. For the ^{7}Be+^{27}Al system, the fusion cross-section was determined by subtracting the measured one-proton stripping cross-section from the total reaction cross-section. Importantly, this approach yields an upper limit for the total fusion cross-section, with values of 635 ± 76, 858 ± 94, and 922 ± 92 mb at laboratory energies of E_{lab} = 17, 19, and 21 MeV, respectively. For the ^{7}Be+^{58}Ni system, the fusion cross-sections were deduced by measuring the fusion-evaporation protons at the center-of-mass energies $E_{\mathrm{c.m.}}$ of 13.9, 15.0, 16.6, 17.4, 17.9, and 19.0 MeV. The resultant total fusion cross-sections were 26 ± 3, 61 ± 7, 165 ± 32, 246 ± 78, 292 ± 46, and 395 ± 116 mb, respectively. Intriguingly, an enhancement relative to the predictions of the one-dimensional barrier-penetration model was observed, even for energies above the barrier. For the ^{7}Be+^{238}U case, the fusion-fission events were measured. In addition, several coincident events of ^{3,4}He-fission fragments were observed to evaluate the possibility of complete fusion.

A comparative analysis of the fusion reactions induced by ^{7}Be interacting with ^{27}Al, ^{58}Ni, and ^{238}U targets was conducted in Ref. [8] and is shown in Fig. 4. An enhancement in the fusion cross-sections was observed for each of the three datasets at energies below the Coulomb barrier. This

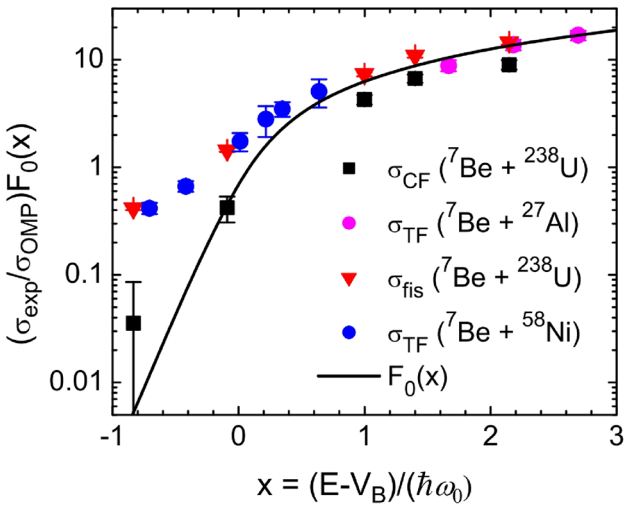

Fig. 4 Reduced total fusion cross-sections for ^{7}Be+^{27}Al, ^{58}Ni, and ^{238}U. For the ^{7}Be+^{238}U system, the results of complete fusion (squares) are shown with the total fusion cross-section deduced from the fusion-fission (triangles). The figure is sourced from Ref. [8]

consistent observation across different target nuclei suggests that the enhancement is predominantly attributable to the intrinsic properties of the ^{7}Be projectiles rather than the specific characteristics of the target nuclei employed in these experiments.

3 Experimental results of ^{8}B

Located near the proton drip line, nucleus ^{8}B exhibited an exceedingly small proton-separation energy of only 138 keV, representing a rare instance in which the ground state manifests a proton-halo structure [36].

3.1 Elastic scattering of ^{8}B

In the energy range of interest, the elastic scattering of ^{8}B was measured on targets of ^{12}C [37] and ^{58}Ni [19]. These results are reviewed in Ref. [8]. In this review, we introduce recent elastic-scattering measurements.

3.1.1 ^{8}B+^{64}Zn

The experimental investigation was performed by Spartà et al. [38] at the HIE-ISOLDE facility of CERN [39] using a post-accelerated beam of ^{8}B with an energy of 38.5 MeV. The angular distribution of the elastic scattering of ^{8}B with ^{64}Zn is shown in Fig. 5. By employing a ^{7}Be+p two-cluster structural model for ^{8}B, CDCC calculations were performed to analyze the scattering data. The results of these calculations with and without coupling to the continuum states are presented in Fig. 5 by the solid and dashed curves, respectively. The elastic breakup produces a small suppression of the elastic cross-section, which has a modest influence on the Coulomb-nuclear-interference peak.

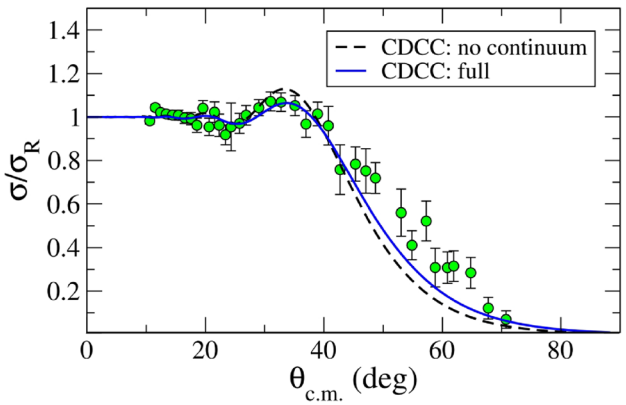

Fig. 5 Elastic-scattering angular distribution of ^{8}B+^{64}Zn at 38.5 MeV. The solid and dashed curves represent the CDCC calculations with and without couplings to the continuum states of ^{8}B. The figure is sourced from Ref. [38]

The total reaction cross-section for the ^{8}B+^{64}Zn system was determined to be 1.5 b, as derived from the CDCC calculation. This value is approximately half of the cross-sections observed for the neutron-halo ^{11}Be+^{64}Zn system at ratios analogous to the center-of-mass energy $E_{\mathrm{c.m.}}$ to the Coulomb-barrier height V_{C}. Notably, the total reaction cross-section for the ^{8}B+^{64}Zn interaction was comparable to that of a stable, weakly bound system of ^{9}Be+^{64}Zn. This intriguing result implies that despite the presence of a proton-halo structure, ^{8}B did not exhibit a pronounced enhancement in reaction activity.

3.1.2 ^{8}B+^{90}Zr

The elastic scattering of ^{8}B+^{90}Zr was measured by Palli et al. [40] at an energy of 26.5 MeV below the Coulomb barrier. The corresponding experimental results are shown in Fig. 6. The results of the full CDCC calculations and CDCC omitting the breakup couplings (one-channel) are shown in Fig. 6 using the dotted-dashed and dotted curves, respectively. The coupling effects, although nonnegligible, are modest compared with neutron-halo nuclear systems.

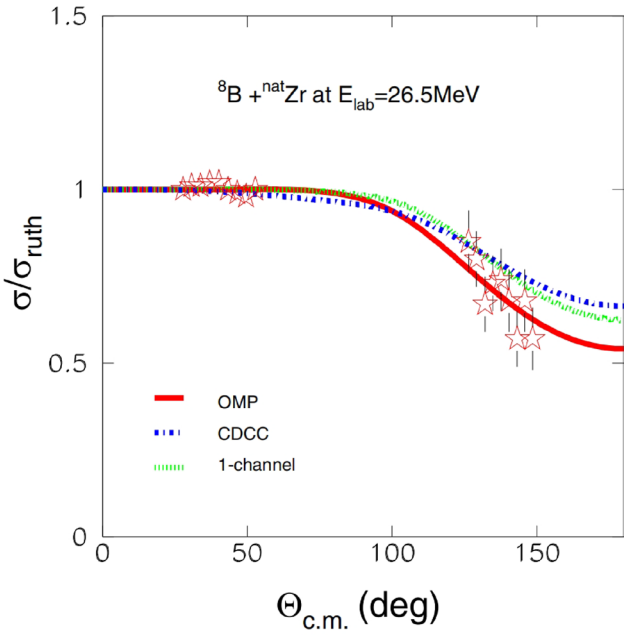

Fig. 6 Elastic-scattering angular distribution of ^{8}B+$^{\mathrm{nat}}$Zr at 26.5 MeV. The solid, dotted-dashed, and dotted curves denote the optical-model calculations with double-folding potentials, and CDCC and one-channel calculations, respectively. The figure is sourced from Ref. [40]

3.1.3 ^{8}B+^{208}Pb

The elastic scattering of ^{8}B+^{208}Pb [41] was measured at 49.4 MeV, and the corresponding angular distribution is shown in Fig. 7. CDCC calculations with and without coupling to the continuum states of ^{8}B are presented along with the data by the solid and dashed curves, respectively. In contrast to the ^{8}B+^{64}Zn and ^{90}Zr systems, CDCC calculations with the ^{7}Be+p structure model provide a relatively poor description of the experimental data (as shown in Fig. 7). This suggests that the structural configuration may be overly simplistic and the possibility of core excitation cannot be ignored [41]. This discrepancy between the light targets and ^{208}Pb target systems may arise from the greater importance of Coulomb interactions in heavy-target systems.

3.2 Breakup reactions of ^{8}B

To date, only a few inclusive measurements have been reported for the breakup reactions of ^{8}B.

The first experiment was performed in 2000 [42] for ^{8}B+^{58}Ni at an incident energy of 25.8 MeV. A subsequent experiment was performed by Aguilera et al. [43] at energies of 25.0, 26.9, and 28.4 MeV. CDCC calculations provide a good description of the inclusive ^{7}Be angular distributions, indicating the predominance of the elastic breakup (EBU) during the direct reaction.

The inclusive measurements of ^{8}B+^{64}Zn [38] and ^{8}B+^{208}Pb [44] were performed at an energy of approximately 1.5 times the Coulomb barrier and at a deep sub-barrier energy, respectively. The inclusive angular distributions of ^{7}Be were successfully reproduced by CDCC calculations. For the ^{8}B+^{64}Zn system, the energy distribution of ^{7}Be was extracted to gain insight into the intricate dynamics of the breakup processes and post-acceleration effects. However, the complexity of the breakup dynamics of ^{8}B is evident using the CDCC and distorted-wave Born approximation calculations. These results indicate that various factors may influence the ^{7}Be energy distributions such as different Coulomb multipoles in the breakup process and their interference, as well as nuclear effects. For ^{8}B+^{208}Pb, the breakup cross-section was determined to be 326 ± 84 mb, which exhausts the total reaction cross-section for this system at an energy well below the barrier.

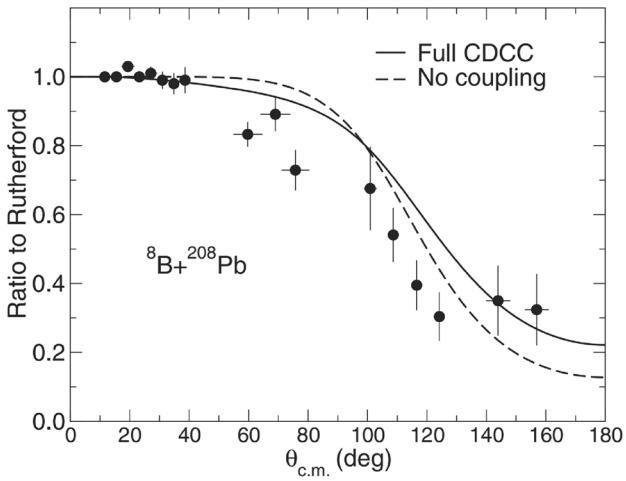

Fig. 7 Elastic-scattering angular distribution of ^{8}B+^{208}Pb system at a beam energy of 50 MeV. The solid and dashed curves denote the results of the CDCC and no-coupling calculations, respectively. The figure is sourced from Ref. [41]

3.3 Fusion reactions of ^{8}B

The total fusion reaction cross-section of ^{8}B+^{58}Ni was determined by measuring the fusion-evaporated protons at ten energies near and below the Coulomb barrier [46]. Subsequently, the results for ^{8}B+^{28}Si were reported for four energies above the Coulomb barrier by measuring the fusion-evaporated alpha particles [47]. The data for ^{8}B+^{58}Ni showed a strong fusion enhancement at all energies, even above the Coulomb barrier. This contrasts with the results of neutron-halo systems, as well as the data for ^{8}B+^{28}Si, whose total fusion cross-sections were suppressed above the barrier.

Recently, direct measurements of the total fusion cross-section for ^{8}B+^{40}Ar were performed by Zamora et al. [45] using an active-target technique. The fusion cross-sections were determined by directly measuring the fusion-evaporation residue directly using a gas-filled time-projection chamber. The reduced fusion-excitation function of ^{8}B+^{40}Ar and the results for ^{8}B+^{28}Si and ^{58}Ni are shown in Fig. 8. The data for ^{8}B+^{40}Ar were systematically consistent with the results for ^{8}B+^{28}Si, showing a suppression of the total fusion cross-section above the Coulomb barrier. Further theoretical and experimental studies are required to understand the observed fusion enhancement above this barrier for the ^{8}B+^{58}Ni system.

4 Experimental results of ^{17}F

^{17}F, which is also a proton drip-line nucleus, features a low breakup threshold (0.6 MeV), which leads to a ^{16}O+p configuration. The first excited state ($E_{\mathrm{ex.}} = 495$ keV, $J^{\pi} = 1/2^{+}$) of ^{17}F presents a proton-halo structure bound by only 105 keV [48].

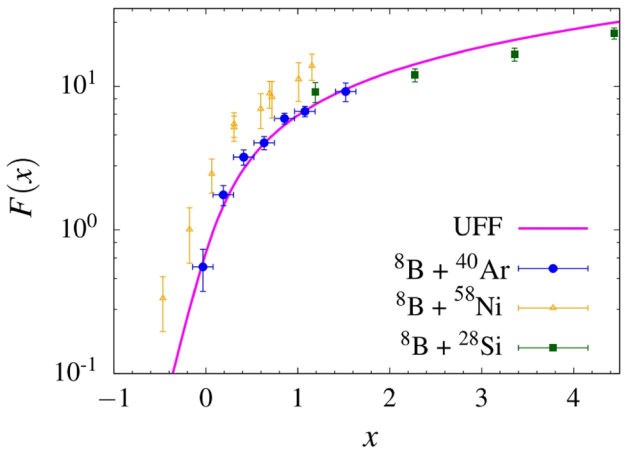

Fig. 8 Reduced total fusion cross-sections of ^{8}B+^{40}Ar (circles), ^{28}Si (squares), and ^{58}Ni (triangles). The solid curve (universal fusion function, UFF) corresponds to the prediction from the one-dimensional barrier-penetration model. The figure is sourced and modified from Ref. [45]

4.1 Elastic scattering of ^{17}F

Several datasets on the elastic scattering of ^{17}F at near-barrier energies have been reported, including ^{17}F+^{12}C at 60.0 MeV [49], ^{17}F+^{58}Ni at 54.1 and 58.5 MeV [50], and ^{17}F+^{208}Pb at 90.4 MeV [51]. The results were reviewed in Ref. [8]. In this section, we focus on two elastic-scattering measurements of ^{17}F+^{89}Y at 50.0 and 59.0 MeV [52] and ^{17}F+^{208}Pb at 94.5 MeV [53] performed by our group in recent years.

4.1.1 ^{17}F+^{89}Y

The elastic scattering of ^{17}F and ^{89}Y was measured at laboratory energies of 50 and 59 MeV using RIBLL1 [52]. The experimental setup included two multiwire proportional chambers to track the beam trajectory and an array of four sets of $\Delta E - E$ silicon-detector telescopes symmetrically installed along the beam line. The angular distributions of elastic scattering are shown in Fig. 9, where the error bars consider only statistical uncertainties. Notably, the energy resolution of the detectors was insufficient to distinguish between the first excited state and ground state of ^{17}F. Consequently, the collected data must be considered as quasi-elastic scattering data.

CDCC calculations were performed to evaluate the influence of the coupling effects on the continuum states. The results are shown by the solid curves in Fig. 9. In Fig. 9a, the CDCC prediction is in good agreement with the data at 50 MeV. In Fig. 9b, the CDCC calculation

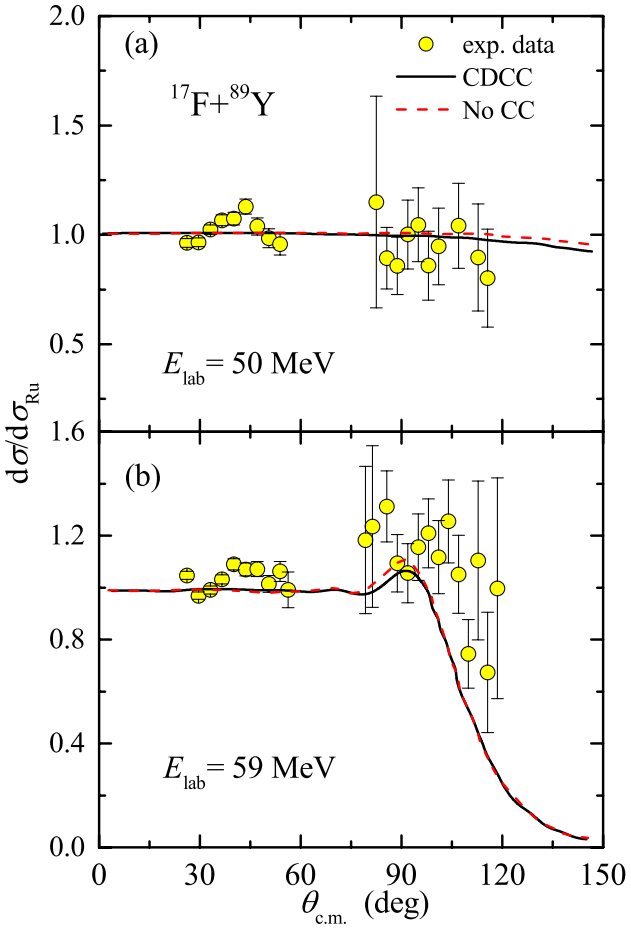

Fig. 9 Angular distributions of elastic scattering of ^{17}F on ^{89}Y at **a** E_{lab} = 50 MeV and **b** 59 MeV. The solid circles show the experimental data. The solid curves represent calculation results with the CDCC approach, while the dashed curves denote the results without continuum–continuum couplings. The figures are sourced from Ref. [52]

provides a good description of the data for the forward angles. However, a slight discrepancy was observed in the backward angles. For comparison, the results that exclude any coupling to the continuum states are illustrated by the dashed curves in Fig. 9. The analysis indicated that the effect of coupling to the continuum states on scattering was insignificant. Furthermore, at backward angles, the coupling introduced an amplification that was considered negligible within the observed scattering-angular distributions.

To address the observed divergence between the elastic-scattering data at 59 MeV and predictions of the CDCC calculations, the potential impact of the one-proton-transfer reaction ^{89}Y(^{17}F,^{16}O)^{90}Zr on the angular distribution of elastic scattering was investigated. This investigation was performed using the coupled reaction channels (CRC) approach, and the results are shown in Fig. 10. In this figure, the CRC results are compared with

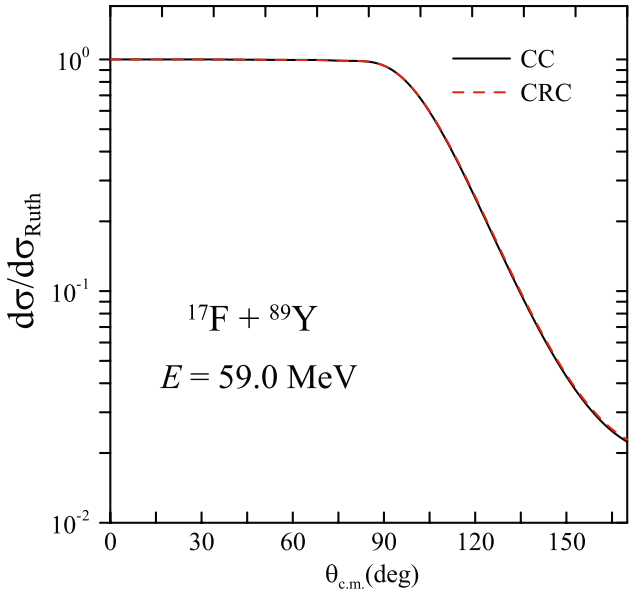

Fig. 10 Comparison of CRC (dashed curve) and CC (solid curve) results for the elastic-scattering angular distributions for $E_{lab}(^{17}F) = 59$ MeV. The figure is sourced and modified from Ref. [52]

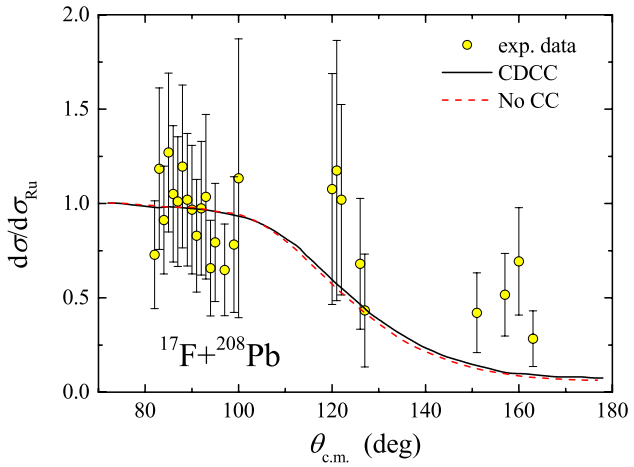

Fig. 11 Quasi-elastic-scattering angular distribution of $^{17}F+^{208}Pb$ at 94.5 MeV. The solid circles are the experimental data. The solid and dashed curves represent the CDCC calculations with and without coupling to the continuum states, respectively. The results are sourced from Ref. [53]

those derived from coupled-channel (CC) calculations in which the coupling to the one-proton-transfer channels were omitted. The results indicated that the one-proton-transfer reaction does not significantly affect the elastic scattering within the energy range.

4.1.2 $^{17}F+^{208}Pb$

The quasi-elastic scattering of $^{17}F+^{208}Pb$ was measured at an incident energy of 94.5 MeV at RIBLL1 [53]. The angular distribution of quasi-elastic scattering is shown in Fig. 11. CDCC calculations were performed to theoretically interpret the scattering data. The results are presented in Fig. 11 using a solid curve. For comparison, the calculation results that omit the coupling to the continuum states are indicated by dashed curves. Coupling to the continuum states of ^{17}F has a negligible effect on elastic scattering.

The influences of inelastic scattering and the one-proton-transfer reaction on the elastic-scattering process were investigated using the CC and CRC calculations, respectively. In the CC calculations, consideration was given to the first excited state of ^{17}F, as well as the excited states 3^- (2.614 MeV), 5^- (3.197 MeV), and 2^+ (4.085 MeV) of ^{208}Pb. These results indicated that the incorporation of the first excited state of ^{17}F, which was treated as a collective state within the CC framework, significantly influenced the elastic scattering. Conversely, coupling originating from the target nucleus exhibited a moderate effect. To delve deeper into the impact of the one-proton stripping reaction on elastic scattering, CRC calculations were performed using the São Paulo potential [54]. The results revealed that the influence of the one-proton-transfer channel on the elastic angular distribution was negligible. Expanding the investigation beyond the one-proton transfer reaction, the contributions of one-neutron-, two-neutron-, and alpha-transfer channels to the quasi-elastic scattering were also evaluated within the CC and CRC frameworks. These results suggest that transfer channels did not affect the measured scattering data significantly.

4.2 Breakup reactions of ^{17}F

Liang et al. [55] performed coincident measurements to elucidate the breakup mechanisms of $^{17}F+^{58}Ni$ and ^{208}Pb systems at an incident energy of 10 MeV per nucleon. For the $^{17}F+^{208}Pb$ system, theoretical analyses concluded that proton stripping is the primary direct reaction procedure. Additionally, the experimental data indicated that the breakup cross-section of ^{17}F is relatively modest. This raises the question of its potential to significantly influence the fusion process, which requires further in-depth investigation. In a subsequent study, Kucuk and Moro [17] performed CDCC calculations and compared their results with experimental data, as shown in Fig. 12. The analysis revealed that for the $^{17}F+^{58}Ni$ system, the CDCC calculation is in good agreement with the experimental data.

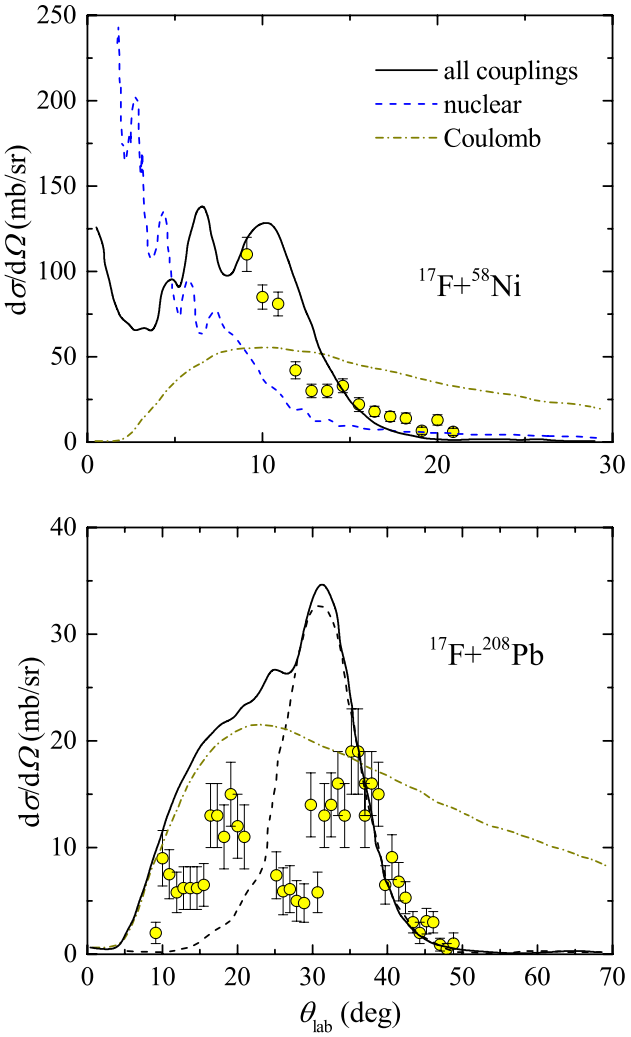

Fig. 12 Nuclear (dashed) and Coulomb (dotted-dashed) contributions to the exclusive breakup cross-section of ^{17}F+^{58}Ni (upper panel) and ^{208}Pb (lower panel). The solid line is the full CDCC calculation, including both nuclear and Coulomb couplings. The figures are sourced from Ref. [17]

However, for the ^{17}F+^{208}Pb system, pronounced divergence was observed between the theoretical predictions and experimental angular distributions, with the theoretical model overestimating the forward-angle data nearly twofold. This discrepancy in the ^{17}F+^{208}Pb system may be attributed to the omission of the core nucleus excitation in the theoretical model. The CDCC calculations further suggest that at forward angles, the Coulomb breakup constituted the predominant component, whereas the nuclear-breakup component reached its maximum near the grazing angle. In addition, the calculations revealed that the Coulomb-polarization effect suppressed the breakup probability.

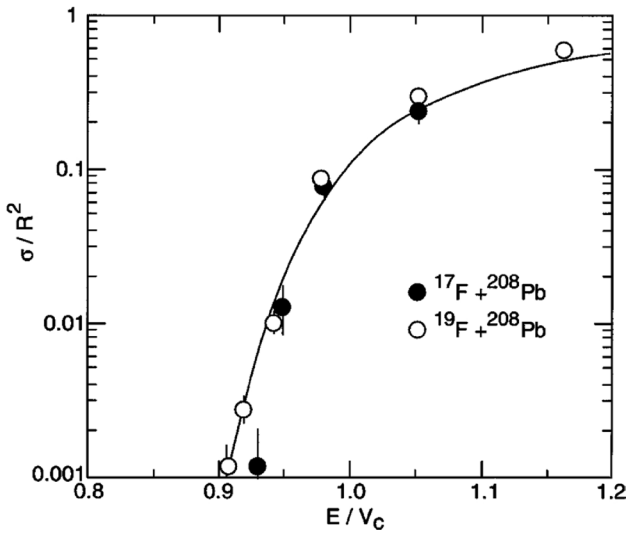

Fig. 13 Reduced fusion-excitation functions of ^{17}F (full circles) and ^{19}F (hallow circles)+^{208}Pb. The solid line indicates the cross-sections measured for ^{19}F+^{208}Pb. The figure is sourced from Ref. [56]

4.3 Fusion reactions of ^{17}F

Fusion cross-section measurements for the ^{17}F+^{208}Pb system [56] were performed. This fusion cross-section was determined through the coincident measurement of fission fragments at four energies ranging from 87 to 99 MeV. The reduced fusion-excitation function for the ^{17}F+^{208}Pb system is illustrated in Fig. 13 and is compared with the corresponding data for the ^{19}F+^{208}Pb system. The fusion behaviors of the two systems are strikingly similar, implying that the weakly bound characteristics of ^{17}F has a minimal impact on the fusion process.

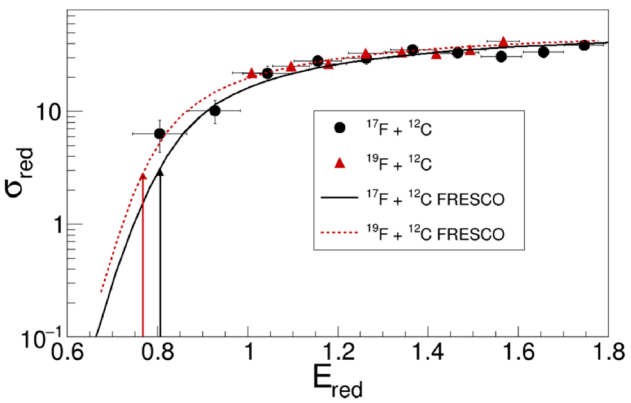

Fig. 14 Comparisons of reduced total fusion cross-sections for the ^{17,19}F+^{12}C systems. The lines denote the results of the no-coupling barrier-penetration calculations using double-folded real potentials for the corresponding systems. The arrows represent the heights of the fusion barriers. The figure is sourced from Ref. [57]

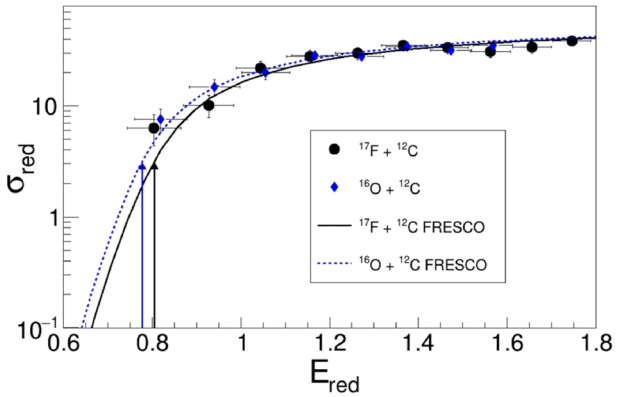

Fig. 15 Similar to Fig. 14, but for the systems of ^{17}F and ^{16}O+^{12}C. The figure is sourced from Ref. [57]

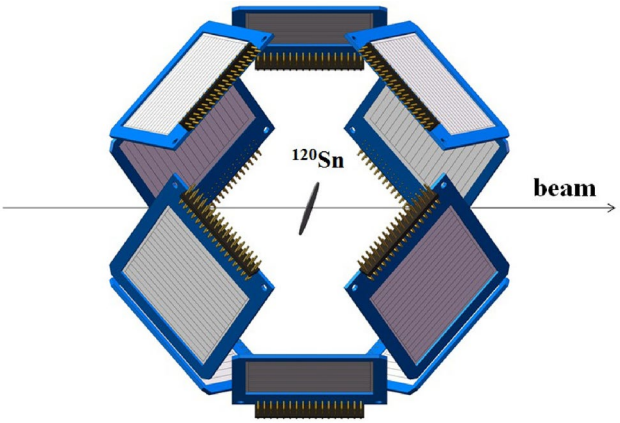

Fig. 16 Schematic of the silicon-detector array STARE used for the ^{8}B+^{120}Sn measurement

A recent experimental investigation by Asher et al. [57] successfully measured the fusion-reaction cross-section of ^{17}F+^{12}C utilizing a 69.1 MeV ^{17}F beam. The total fusion-reaction cross-section for this system was determined by measuring the fusion-evaporation residues, by employing the Encore active-target detector [58]. In a comparative study, the fusion cross-sections of stable systems ^{16}O+^{12}C and ^{19}F+^{12}C were also measured. The reduced total fusion-reaction cross-sections for these three systems are presented in Figs. 14 and 15. ^{17}F exhibits a fusion behavior similar to that of its stable counterparts ^{16}O and ^{19}F. This observation is particularly noteworthy, as it suggests that neither the weak binding nor the halo-like characteristics of the first excited state of ^{17}F significantly influence the total fusion-excitation function above the Coulomb barrier.

5 Complete kinematics measurement of ^{8}B and ^{17}F

From an experimental perspective, an essential approach toward obtaining a thorough understanding of the breakup dynamics requires the coincident measurement of breakup fragments. This approach enables the detailed characterization of breakup reactions by analyzing the energy and angular correlations between the breakup fragments. Despite concerted efforts dedicated to this endeavor, the limited beam intensity and inadequate detection efficiency have hindered the realization of coincident measurements for the ^{8}B and ^{17}F systems. We performed the first complete kinematics measurements of ^{8}B+^{120}Sn [59] and ^{17}F+^{58}Ni [60] to elucidate the reactions induced by the proton drip-line nuclei.

5.1 Detector arrays

Detector arrays with high detection efficiency are essential for performing complete kinematics measurements, particularly for radioactive ion beams with low intensities. Two detector arrays, the silicon telescope array of the Silicon Telescopic Array for Reactions induced by Exotic nuclei (STARE) [61] and the ionization chamber array of the Multilayer Ionization-chamber Telescope Array (MITA) [62], were designed for the measurements of ^{8}B and ^{17}F, respectively. Homemade preamplifiers [63] have been employed to further improve the signal-to-noise ratio.

For the ^{8}B+^{120}Sn measurements, the reaction products were identified using silicon telescopes. Therefore, a silicon detector array (STARE) was constructed to cover a large solid angle. STARE is composed of ten silicon telescopes arranged in a spherical shape with an approximate radius of 70 mm. A schematic of STARE is shown in Fig. 16. Each telescope of STARE has three stages of silicon detectors: the first layer is a 40/60 μm double-sided silicon-strip detector (DSSD) with an effective area of 50 mm × 50 mm, followed by two layers of quadrant silicon detectors (QSDs) with thicknesses of 1000/1500 μm. STARE covers approximately 40% of the total solid angle, offering an angular coverage spanning 24°−158° with an angular resolution of approximately ±1.23°.

Silicon telescopes are unsuitable for the ^{17}F+^{58}Ni system, characterized by relatively heavy reaction products with low energies because of the potential energy loss of the heavy reaction products within the first detector layer, which impedes accurate particle identification. Consequently, MITA, an array based on an ionization chamber, was used for the ^{17}F+^{58}Ni measurement. MITA also comprises ten telescopic units, each composed of four detection layers: an ionization chamber, a 40 (or 60)-μm DSSD, and

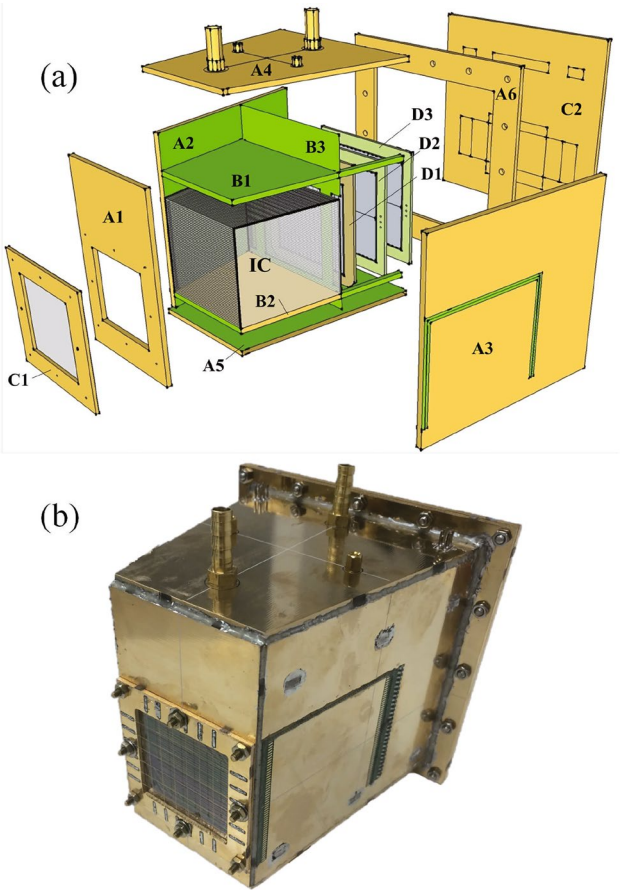

Fig. 17 **a** Schematic of the structure of each unit of MITA. **b** Photograph of one unit. These figures are sourced from Ref. [62]

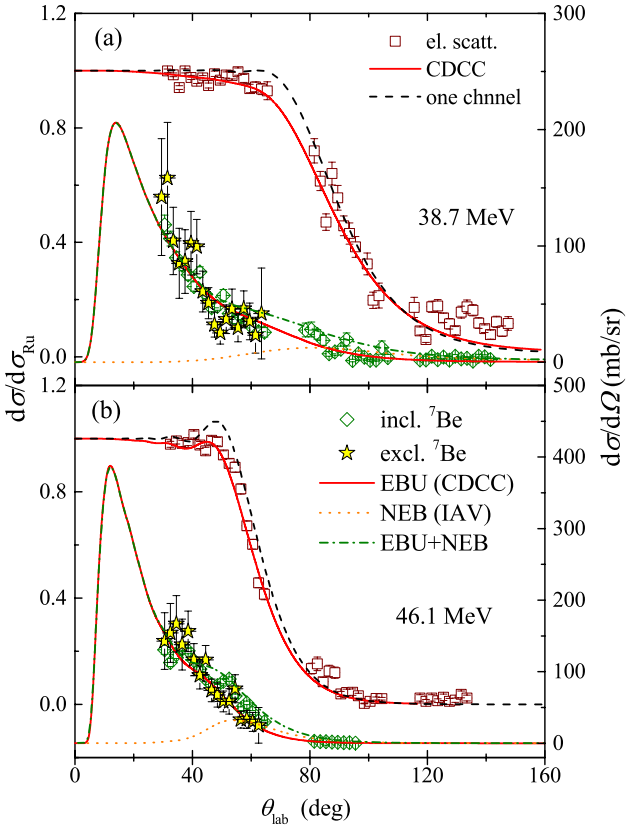

Fig. 18 Angular distributions of elastic scattering and inclusive and exclusive breakup at **a** 38.7 and **b** 46.1 MeV, which are denoted by squares, diamonds, and stars, respectively. The elastic-scattering and breakup data are respectively related to the left and right axes. CDCC calculations for elastic scattering and EBU are represented by solid curves. The one-channel calculations for the elastic scattering are shown by the dashed curves. The dotted lines correspond to the IAV model results for NEB contributions. The dash-dotted lines denote the sum of EBU and NEB. The figures are sourced and modified from Ref. [59]

two QSDs with thicknesses of 300 µm and 1000 (or 1500) µm. The schematic of the structure of each unit of MITA is shown in Fig. 17.

Both STARE and MITA have excellent particle-identification capabilities, as demonstrated in Refs. [59, 60, 62].

5.2 ^{8}B+^{120}Sn measurement

The experiment was performed at the low-energy radioactive ion beam facility, the Radioactive Ion Beam Separator (CRIB) [64] of the Center for Nuclear Study, University of Tokyo. Secondary ^{8}B beams were produced with two energies (37.8 ± 0.5 and 46.1 ± 0.6 MeV) around the Coulomb barrier with an intensity of approximately 10^4 pps and a purity of $\sim 20\%$.

The angular distributions of elastic scattering relative to Rutherford scattering for the two distinct measured energies are depicted in Fig. 18a, b, as denoted by the squares. The calculation results from the CDCC approach are represented by solid curves in the same figure. These theoretical curves are in good agreement with the experimental data. Furthermore, Fig. 18 also presents the results of the one-channel calculations, denoted by dashed curves. In these calculations, couplings to the continuum states were excluded. A comparative analysis of these results with the CDCC calculations revealed that the influence of the continuum states on elastic scattering is insignificant.

Angular distributions for the exclusive and inclusive measurements of ^{7}Be are shown in Fig. 18, which are distinguished by stars and diamonds, respectively. These datasets revealed a concordance between them, well within the bounds of experimental uncertainty. This congruence, observed for the first time, offers clear experimental evidence that the production of ^{7}Be is predominantly dictated by breakup processes rather than proton-transfer mechanisms.

Calculations employing the CDCC and Ichimura, Austern, and Vincent (IAV) models [65] were performed to evaluate the individual contributions of the elastic breakup

(EBU) and non-elastic breakup (NEB) for direct reactions. The CDCC and IAV results are shown in Fig. 18, represented by the solid and dotted curves, respectively. The sum of the CDCC and IAV calculations, referred to as the total breakup (TBU), is shown in Fig. 18 as a dotted-dashed curve. The inclusive breakup angular distribution can be properly described using the TBU curve. The cross-sections for EBU and NEB, as derived from the calculations, were determined to be $\sigma_{\mathrm{EBU}} = 351.5\,(420.5)$ mb and $\sigma_{\mathrm{NEB}} = 78.3\,(91.4)$ mb at an energy of 38.7 (46.1) MeV, respectively. These results clearly demonstrate that while the NEB contribution is nonnegligible, it represents a relatively modest fraction, approximately 18%, of the total ^{7}Be yield.

The reconstructed relative-energy distribution E_{rel} of the breakup fragments resulting from the ^{7}Be+ p reaction at 38.7 MeV is shown in Fig. 19a. The solid curves represent the simulation based on the outputs of the CDCC, which reproduced the experimental data well. A peak in the E_{rel} spectrum, located at an energy of approximately 0.6 MeV, has been observed. This energy corresponds closely to the first resonance state of ^{8}B ($E_{\mathrm{ex.}} = 0.77$ MeV, $J^{\pi} = 1^{+}$, $\Gamma = 35.6$ keV). Using a CDCC-based simulation, the contribution of this 1^{+} resonance to the breakup process was evaluated and quantified as $(4.4 \pm 2.0)\%$ at 38.7 MeV. At a higher energy of 46.1 MeV, the contribution of this resonance was determined to be $(3.8 \pm 2.5)\%$. Considering the lifetime of this resonance, which is on the order of 10^{-20} s, it is sufficiently prolonged to ensure that the breakup occurring via this state is predominantly along the outgoing trajectory, thereby moving away from the target nucleus. However, a modest proportion of the 1^{+} resonance suggests that the prompt component significantly governs the breakup mechanism.

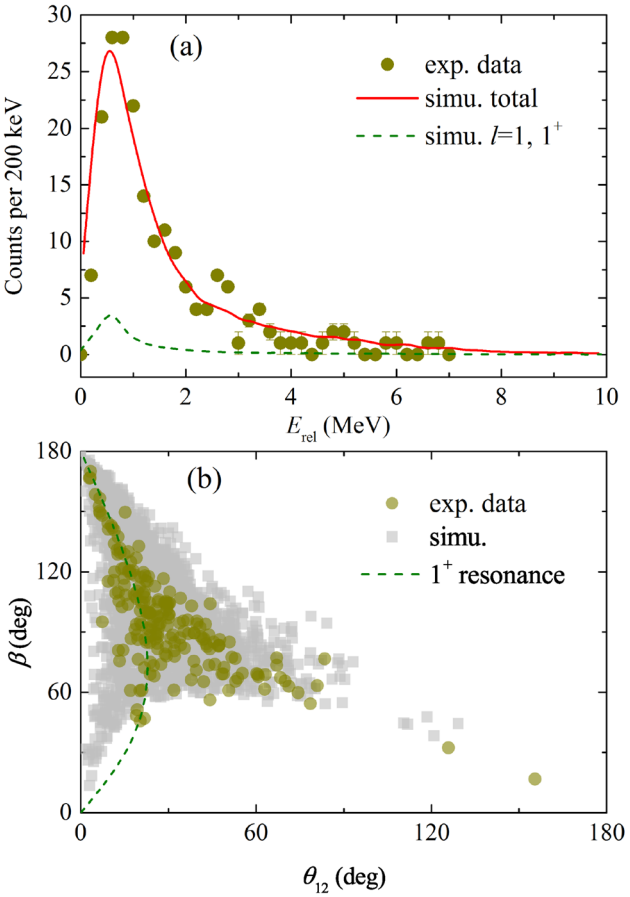

Fig. 19 **a** Measured E_{rel} distribution and **b** angular correlation for breakup fragments ^{7}Be and p from the ^{8}B+^{120}Sn system at 38.7 MeV. Circles denote the experimental data. The solid and dashed curves in **a** represent the simulated distributions of E_{rel} and the contribution of the p-wave 1^{+} state based on the detailed CDCC outputs. The squares in **b** represent the CDCC-based simulation results, and the solid curve denotes the expected β-θ_{12} correlation assuming asymptotic breakup from the 1^{+} resonance of ^{8}B. Figures are sourced and modified from Ref. [59]

Reconstructed correlations of the laboratory opening angle (θ_{12}) and orientation of the relative momentum of the breakup fragments (β) in their center-of-mass frame at 38.7 MeV are shown in Fig. 19b. The dashed line in the figure represents the theoretical correlation anticipated between θ_{12} and β for the asymptotic breakup via the 1^{+} resonant state of ^{8}B [66]. Events that fall along the dashed line indicate the asymptotic nature of the breakup. This implies that the fragments moved beyond the influence of the target Coulomb field, indicative of a distant breakup event. Conversely, breakup events occurring in close proximity to the target nucleus exhibit a perturbed θ_{12}-β correlation, which is attributed to the effects of Coulomb post-acceleration [66]. As depicted in Fig. 19b, a significant divergence of events from the asymptotic limit is observed. This is indicative of the predominance of a near-target breakup. Simulations based on CDCC calculations offer a reasonable description of the θ_{12}-β correlations represented by the squares in the figure. In terms of θ_{12}, the majority of events are concentrated at small angles, with a pronounced peak around 30°. This distinct forward peak of θ_{12} implies that most breakup events, while prompt, occur along the outgoing trajectory. This breakup mechanism can potentially exert a minor impact on the complete fusion cross-section of ^{8}B. Notably, similar results are observed for the case of 46.1 MeV, reinforcing the consistency of the observed phenomena across the different energy regimes.

5.3 ^{17}F+^{58}Ni measurement

We performed the first complete kinematics measurements of ^{17}F interacting with a medium-mass target ^{58}Ni at CRIB [60]. Four distinct energies, 43.6 ± 0.7, 47.5 ± 0.7, 55.7 ± 0.8, and 63.1 ± 0.9 MeV, were achieved in the middle of the target with typical intensities of $6-10 \times 10^{5}$ pps and a purity of approximately 85%. MITA was used for the measurements. Owing to the excellent particle-identification capabilities of MITA, particles as light as protons, deuterons, and alpha particles, and heavier ions, such as ^{16}O and ^{17}F, were unambiguously discerned.

CDCC calculations were performed to interpret the quasi-elastic scattering data. The results indicated that the influence of breakup coupling on elastic scattering was relatively minor, suggesting that these couplings do not significantly influence elastic scattering. The angular distributions of ^{16}O generated by the reaction of ^{17}F+^{58}Ni were subjected to theoretical analysis using both CDCC and IAV model calculations. The results of these calculations demonstrated that exclusive ^{16}O data were reproduced using the CDCC approach. Moreover, the sum contributions of the EBU and NEB, collectively denoted as TBU, provided a good description of both the amplitude and structural features of the inclusive data. The results also indicated that the NEB is the predominant constituent of the total inclusive ^{16}O yield.

The total fusion (TF) cross-sections, represented as σ_{TF}, were determined through an analysis of fusion-evaporation protons and alpha particles, as documented in [62]. A comparative examination of the reduced total-reaction cross-sections σ_R and σ_{TF} are performed for both ^{17}F [60, 67] and ^{16,17}O interacting with a ^{58}Ni target [68–70]. This comparison is presented in Fig. 20a, b. As shown in the figures, the cross-sections of ^{17}F, both σ_R and σ_{TF}, exhibit a similar behavior with those of ^{16}O at energies above the Coulomb barrier. However, a noteworthy divergence was observed in the sub-barrier energy domain, where ^{17}F demonstrates a significant enhancement in the cross-sections.

Excitation functions for the ^{17}F+^{58}Ni system, including the total reaction, exclusive and inclusive breakup processes, and TF, are shown in Fig. 21. Superimposed on this representation is the theoretical predictions of the corresponding reaction channels. The sum of the cross-sections for the inclusive breakup, TF, and excitations to the first excited states of ^{17}F and ^{58}Ni nearly saturated the total-reaction cross-section, leaving minimal space for additional, unaccounted reaction channels.

CDCC calculations were performed to evaluate the influence of breakup on fusion-reaction dynamics. The results of the CDCC calculations are shown in Fig. 21, where the dashed-dotted curve corresponds to the calculations including couplings to the continuum states, and the dashed curve represents calculations exclusive to such couplings. At energies above the Coulomb barrier, the theoretical results are essentially indistinguishable from one another regardless of whether they incorporate couplings to the continuum states. These theoretical predictions were observed to be in good agreement with the experimental fusion cross-sections. By contrast, within the sub-barrier energy region, the experimental data exhibited good agreement with the theoretical description when the couplings to the continuum states were included in the calculations. Calculations that exclude these couplings are prone to a substantial underestimation of the experimental data, thereby highlighting the strong coupling effects of the breakup in fusion reactions below the Coulomb barrier.

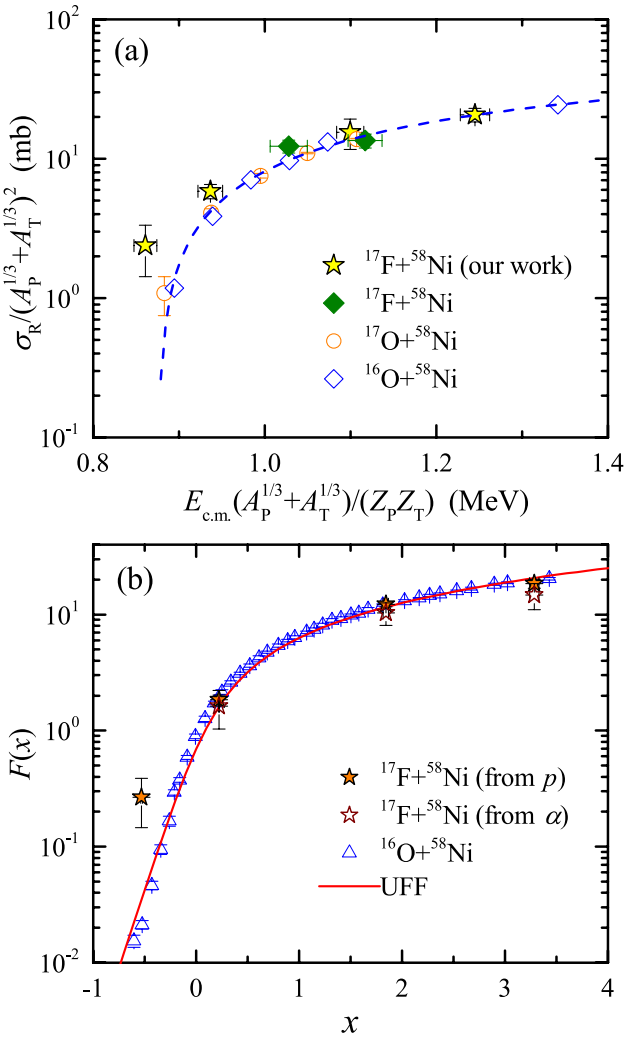

Fig. 20 Comparison of the reduced **a** σ_R and **b** σ_{TF} between ^{17}F+^{58}Ni and oxygen systems. The σ_R of ^{17}F+^{58}Ni, denoted by stars, are from our work [60]. The results of ^{17}F, ^{17}O, and ^{16}O +^{58}Ni, represented by filled diamonds, empty circles, and empty diamonds, are sourced from Refs. [67–69], respectively. The dashed curve in **a** shows the trend of the behavior of ^{16,17}O+^{58}Ni. The filled and empty stars in **b** represent the σ_{TF} of ^{17}F+^{58}Ni deduced from fusion- evaporated protons and alpha particles, respectively. The empty triangles are the results for ^{16}O +^{58}Ni sourced from Ref. [70]. The solid curve in **b** represents the benchmark UFF [71]. The figures are sourced and modified from Ref. [60]

6 Summary and outlook

We reviewed experimental investigations focusing on the reaction mechanisms of proton-rich ^{7}Be, ^{8}B, and ^{17}F systems at energies around the Coulomb barrier. These results highlight the notable differences in the reaction dynamics of these proton-rich systems compared with their neutron-rich counterparts. These disparities manifest in various facets, including moderate coupling effects to the continuum states observed in elastic scattering and the remarkable enhancement of the total fusion

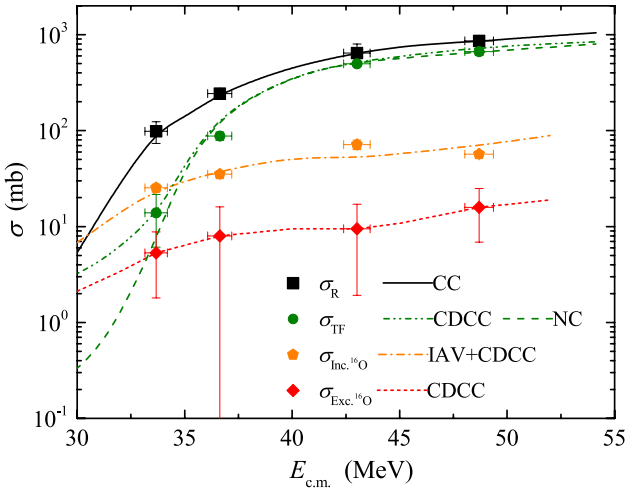

Fig. 21 Excitation functions of total reaction (squares), exclusive (diamonds) and inclusive (triangles) breakups, and the total fusion (TF) deduced from fusion-evaporation protons (circles) of ^{17}F+^{58}Ni. The solid curve denotes the CC calculations for the σ_R. The dash-dotted and dashed curves represent the TF derived from CDCC calculations with and without the continuum couplings, respectively. The dash-dotted and dotted curves are the theoretical results of CDCC plus the IAV model and CDCC, corresponding to the inclusive and exclusive breakup, respectively. The figure is sourced and modified from Ref. [60]

cross-sections, even above the Coulomb barrier. To elucidate the reaction dynamics of proton-rich nuclei, we first performed complete kinematic measurements of the ^{8}B+^{120}Sn and ^{17}F+^{58}Ni systems. Our findings revealed the profound influence of the nuclear structure on the reaction dynamics. Notably, in the case of ^{8}B characterized by a proton-halo structure, elastic breakup emerged as the dominant direct process. The correlations between the breakup fragments of ^{8}B indicated that the continuum states of ^{8}B exert a minor influence on the complete fusion reactions. Conversely, for ^{17}F, which features a valence-proton structure, non-elastic breakup emerged as the primary direct-reaction mechanism. This was accompanied by an enhancement in the fusion cross-sections below the Coulomb barrier, owing to the couplings to the continuum states of ^{17}F. Using the developments in the experimental and theoretical techniques of these works, we can extend these investigations to include light proton-rich nuclei such as ^{7}Be and ^{9,10}C. These forthcoming studies hold immense promise for systematically and comprehensively unraveling the reaction dynamics of proton-rich nuclei, thereby promoting the development of nuclear-reaction theory.

References

1. L.F. Canto, P.R.S. Gomes, R. Donangelo et al., Recent developments in fusion and direct reactions with weakly bound nuclei. Phys. Rep. **596**, 1 (2015). https://doi.org/10.1016/j.physrep.2015.08.001
2. Y. Chen, Y.L. Ye, K. Wei, Progress and perspective of the research on exotic structures of unstable nuclei. Nucl. Tech. (in Chinese) **46**, 080020 (2023). https://doi.org/10.11889/j.0253-3219.2023.hjs.46.080020
3. S. Zhang, Y.F. Geng, F.R. Xu, Ab initio Gamow shell-model calculations for dripline nuclei. Nucl. Tech. (in Chinese) **46**, 080012 (2023). https://doi.org/10.11889/j.0253-3219.2023.hjs.46.080012
4. L. Yang, C.J. Lin, H.M. Jia et al., Progress on nuclear reactions and related nuclear structure at low energies. Nucl. Tech. (in Chinese) **46**, 080006 (2023). https://doi.org/10.11889/j.0253-3219.2023.hjs.46.080006
5. L. Zhou, S.M. Wang, D.Q. Fang et al., Recent progress in two-proton radioactivity. Nucl. Sci. Tech. **33**, 105 (2022). https://doi.org/10.1007/s41365-022-01091-1
6. N. Keeley, R. Raabe, N. Alamanos et al., Fusion and direct reactions of halo nuclei at energies around the Coulomb barrier. Prog. Part. Nucl. Phys. **59**, 579 (2007). https://doi.org/10.1016/j.ppnp.2007.02.002
7. N. Keeley, N. Alamanos, K.W. Kemper et al., Elastic scattering and reactions of light exotic beams. Prog. Part. Nucl. Phys. **63**, 396 (2009). https://doi.org/10.1016/j.ppnp.2009.05.003
8. J.J. Kolata, V. Guimaraes, E.F. Aguilera, Elastic scattering, fusion, and breakup of light exotic nuclei. Eur. Phys. J. A **52**, 123 (2016). https://doi.org/10.1140/epja/i2016-16123-1
9. Ł Standyło, L. Acosta, C. Angulo et al., Breakup and neutron-transfer effects on ^{6}He+^{206}Pb elastic scattering below the coulomb barrier. Phys. Rev. C **87**, 064603 (2013). https://doi.org/10.1103/PhysRevC.87.064603
10. L. Acosta, A.M. Sánchez-Benítez, M.E. Gómez et al., Elastic scattering and α-particle production in ^{6}He+^{208}Pb collisions at 22 Mev. Phys. Rev. C **84**, 044604 (2011). https://doi.org/10.1103/PhysRevC.84.044604
11. M. Cubero, J.P. Fernández-García, M. Rodríguez-Gallardo et al., Do halo nuclei follow Rutherford elastic scattering at energies below the barrier? The case of ^{11}Li. Phys. Rev. Lett. **109**, 262701 (2012). https://doi.org/10.1103/PhysRevLett.109.262701
12. A.D. Pietro, G. Randisi, V. Scuderi et al., Elastic scattering and reaction mechanisms of the halo nucleus ^{11}Be around the Coulomb barrier. Phys. Rev. Lett. **105**, 022701 (2010). https://doi.org/10.1103/PhysRevLett.105.022701
13. A.D. Pietro, V. Scuderi, A.M. Moro et al., Experimental study of the collision ^{11}Be+^{64}Zn around the Coulomb barrier. Phys. Rev. C **85**, 054607 (2012). https://doi.org/10.1103/PhysRevC.85.054607
14. P.A. DeYoung, P.J. Mears, J.J. Kolata et al., Two-neutron transfer in the ^{6}He+^{209}Bi reaction near the Coulomb barrier. Phys. Rev. C **71**, 051601(R) (2005). https://doi.org/10.1103/PhysRevC.71.051601
15. M. Ito, K. Yabana, T. Nakatsukasa et al., Fusion reaction of halo nuclei: a real-time wave-packet method for three-body tunneling dynamics. Nucl. Phys. A **787**, 267 (2007). https://doi.org/10.1016/j.nuclphysa.2006.12.042
16. E.F. Aguilera, P. Amador-Valenzuela, E. Martinez-Quiroz et al., Above-barrier fusion enhancement of proton-halo systems.

Phys. Rev. C **93**, 034613 (2016). https://doi.org/10.1103/PhysRevC.93.034613
17. Y. Kucuk, A.M. Moro, Exclusive breakup of ^{17}F on ^{58}Ni and ^{208}Pb within the continuum-discretized coupled-channels method. Phys. Rev. C **86**, 034601 (2012). https://doi.org/10.1103/PhysRevC.86.034601
18. M. Mazzocco, D. Torresi, D. Pierroutsakou et al., Direct and compound-nucleus reaction mechanisms in the ^{7}Be+^{58}Ni system at near-barrier energies. Phys. Rev. C **92**, 024615 (2015). https://doi.org/10.1103/PhysRevC.92.024615
19. E.F. Aguilera, E. Martinez-Quiroz, D. Lizcano et al., Reaction cross sections for ^{8}B, ^{7}Be, and ^{6}Li+^{58}Ni near the Coulomb barrier: proton-halo effects. Phys. Rev. C **79**, 021601(R) (2009). https://doi.org/10.1103/PhysRevC.79.021601
20. J. Cook, Global optical-model potentials for the elastic scattering of ^{6,7}Li projectiles. Nucl. Phys. A **388**, 153 (1982). https://doi.org/10.1016/0375-9474(82)90513-9
21. L.L. Lee Jr., J.P. Schiffer, Studies of elastic scattering of protons, deuterons, and alpha particles from isotopes of Cu, Ni, and Fe. Phys. Rev. B **134**, 765 (1964). https://doi.org/10.1103/PhysRev.134.B765
22. D. Fick, R.E. Brown, W. Grüebler et al., Elastic scattering of polarized tritons from ^{12}C, ^{15}V, and ^{58}Ni at 9 and 11 MeV. Phys. Rev. C **29**, 324 (1984). https://doi.org/10.1103/PhysRevC.29.324
23. B. Buck, A.C. Merchant, Cluster model of $a = 7$ nuclei revisited, and the astrophysical s factors for ^{3}He$(\alpha,\gamma)^{7}$Be and ^{3}H$(\alpha,\gamma)^{7}$Li at zero energy. J. Phys. G: Nucl. Phys. **14**, L211 (1988). https://doi.org/10.1088/0305-4616/14/10/002
24. W.L. Zhan, Z.Y. Guo, G.H. Liu et al., Radioactive ion beam line in Lanzhou. Sci. China Ser. A-Math. **42**, 528 (1999). https://doi.org/10.1007/BF02882249
25. Z. Sun, W.L. Zhan, Z.Y. Guo et al., RIBLL, the radioactive ion beam line in Lanzhou. Nucl. Instrum. Methods Phys. Res. Sect. A **503**, 496 (2003). https://doi.org/10.1016/S0168-9002(03)01005-2
26. W.D. Chen, H.R. Guo, T. Ye et al., Application of the Lagrange-mesh method in continuum-discretized coupled-channel calculations. J. Phys. G: Nucl. Part. Phys. **49**, 075104 (2022). https://doi.org/10.1088/1361-6471/ac7249
27. S. Schiffmann, L. Filippin, D. Baye et al., POLALMM: a program to compute polarizabilities for nominal one-electron systems using the Lagrange-mesh method. Comput. Phys. Commun. **256**, 107452 (2020). https://doi.org/10.1016/j.cpc.2020.107452
28. S.R. Hilfer, J.J.W. Yang, Accumulation of CPC-precipitable material at apical cell surfaces during formation of the optic cup. Anat. Rec. **197**, 423 (1980). https://doi.org/10.1002/ar.1091970406
29. V. Avrigeanu, M. Avrigeanu, C. Mănăilescu, Further explorations of the α-particle optical model potential at low energies for the mass range $A \approx 45 - 209$. Phys. Rev. C **90**, 044612 (2014). https://doi.org/10.1103/PhysRevC.90.044612
30. D.Y. Pang, P. Roussel-Chomaz, H. Savajols et al., Global optical model potential for $A = 3$ projectiles. Phys. Rev. C **79**, 024615 (2009). https://doi.org/10.1103/PhysRevC.79.024615
31. M. Mazzocco, N. Keeley, A. Boiano et al., Elastic scattering for the ^{8}B and ^{7}Be+^{208}Pb systems at near-Coulomb barrier energies. Phys. Rev. C **100**, 024602 (2019). https://doi.org/10.1103/PhysRevC.100.024602
32. H. Amro, F.D. Becchetti, Y. Chen et al., ^{7}Be-induced α-transfer reaction on ^{12}C. Eur. Phys. J. ST **150**, 1 (2007). https://doi.org/10.1140/epjst/e2007-00250-4
33. K. Kalita, S. Verma, R. Singh et al., Elastic scattering and fusion cross sections for ^{7}Be, ^{7}Li+^{27}Al systems. Phys. Rev. C **73**, 024609 (2006). https://doi.org/10.1103/PhysRevC.73.024609
34. E. Martinez-Quiroz, E.F. Aguilera, D. Lizcano et al., Near- and sub-barrier fusion of the ^{7}Be+^{58}Ni system. Phys. Rev. C **90**, 014616 (2014). https://doi.org/10.1103/PhysRevC.90.014616
35. R. Raabe, C. Angulo, J.L. Charvet et al., Fusion and direct reactions around the barrier for the systems ^{7,9}Be, ^{7}Li+^{238}U. Phys. Rev. C **74**, 044606 (2006). https://doi.org/10.1103/PhysRevC.74.044606
36. G.A. Korolev, A.V. Dobrovolsky, A.G. Inglessi et al., Halo structure of ^{8}B determined from intermediate energy proton elastic scattering in inverse kinematics. Phys. Lett. B **780**, 200 (2018). https://doi.org/10.1016/j.physletb.2018.03.013
37. A. Barioni, J.C. Zamora, V. Guimaraes et al., Elastic scattering and total reaction cross sections for the ^{8}B, ^{7}Be, and ^{6}Li+^{12}C systems. Phys. Rev. C **84**, 014603 (2011). https://doi.org/10.1103/PhysRevC.84.014603
38. R. Spartà, A.D. Pietro, P. Figuera et al., Probing proton halo effects in the ^{8}B+^{64}Zn collision around the Coulomb barrier. Phys. Lett. B **820**, 136477 (2021). https://doi.org/10.1016/j.physletb.2021.136477
39. Y. Kadi, Y. Blumenfeld, W.V. Delsolaro et al., Post-accelerated beams at isolde. J. Phys. G: Nucl. Part. Phys. **44**, 084003 (2017). https://doi.org/10.1088/1361-6471/aa78ca
40. K. Palli, A. Pakou, P.D. O'Malley et al., Elastic scattering of ^{8}B+^{nat}Zr at the sub-barrier energy of 26.5 MeV. Phys. Rev. C **109**, 064614 (2024). https://doi.org/10.1103/PhysRevC.109.064614
41. M. Mazzocco, N. Keeley, A. Boiano et al., Elastic scattering for the ^{8}B and ^{7}Be+^{208}Pb systems at near-Coulomb barrier energies. Phys. Rev. C **100**, 024602 (2019). https://doi.org/10.1103/PhysRevC.100.024602
42. V. Guimaraes, J.J. Kolata, D. Peterson et al., Nuclear and coulomb interaction in ^{8}B breakup at sub-Coulomb energies. Phys. Rev. Lett. **84**, 1862 (2000). https://doi.org/10.1103/PhysRevLett.84.1862
43. E.F. Aguilera, E. Martinez-Quiroz, T.L. Belyaeva et al., New measurements on breakup of ^{8}B+^{58}Ni at energies around the Coulomb barrier. Phys. At. Nucl. **71**, 1163 (2008). https://doi.org/10.1134/S1063778808070065
44. A. Pakou, L. Acosta, P.D. O'Malley et al., Dominance of direct reaction channels at deep sub-barrier energies for weakly bound nuclei on heavy targets: the case ^{8}B+^{208}Pb. Phys. Rev. C **102**, 031601(R) (2020). https://doi.org/10.1103/PhysRevC.102.031601
45. J.C. Zamora, V. Guimaraes, G.V. Rogachev et al., Direct fusion measurement of the ^{8}B proton-halo nucleus at near-barrier energies. Phys. Lett. B **816**, 136256 (2021). https://doi.org/10.1016/j.physletb.2021.136256
46. E.F. Aguilera, P. Amador-Valenzuela, E. Martinez-Quiroz et al., Near-barrier fusion of the ^{8}B+^{58}Ni proton-halo system. Phys. Rev. Lett. **107**, 092701 (2011). https://doi.org/10.1103/PhysRevLett.107.092701
47. A. Pakou, E. Stiliaris, D. Pierroutsakou et al., Fusion cross sections of ^{8}B+^{28}Si at near-barrier energies. Phys. Rev. C **87**, 014619 (2013). https://doi.org/10.1103/PhysRevC.87.014619
48. R. Lewis, A.C. Hayes, Deuteron stripping as a probe of the proton halo in ^{17}F. Phys. Rev. C **59**, 1211 (1999). https://doi.org/10.1103/PhysRevC.59.1211
49. G.L. Zhang, C.L. Zhang, H.Q. Zhang et al., Quasi-elastic scattering of the proton drip line nucleus ^{17}F on ^{12}C at 60 MeV. Eur. Phys. J. A **48**, 65 (2012). https://doi.org/10.1140/epja/i2012-12065-x
50. M. Mazzocco, C. Signorini, D. Pierroutsakou et al., Reaction dynamics for the system ^{17}F+^{58}Ni at near-barrier energies. Phys. Rev. C **82**, 054604 (2010). https://doi.org/10.1103/PhysRevC.82.054604
51. M. Romoli, E. Vardaci, M.D. Pietro et al., Measurements of ^{17}F scattering by ^{208}Pb with a new type of large solid angle detector

array. Phys. Rev. C **69**, 064614 (2004). https://doi.org/10.1103/PhysRevC.69.064614
52. G.L. Zhang, G.X. Zhang, C.J. Lin et al., Angular distribution of elastic scattering induced by ^{17}F on medium-mass target nuclei at energies near the coulomb barrier. Phys. Rev. C **97**, 044618 (2018). https://doi.org/10.1103/PhysRevC.97.044618
53. C.H. Rong, J. Rangel, Y.S. Wu et al., Study of quasi-elastic scattering of ^{17}F+^{208}Pb at energies around Coulomb barrier. Eur. Phys. J. A **57**, 143 (2021). https://doi.org/10.1140/epja/s10050-021-00454-3
54. L.C. Chamon, D. Pereira, M.S. Hussein et al., Nonlocal description of the nucleus–nucleus interaction. Phys. Rev. Lett. **79**, 5218 (1997). https://doi.org/10.1103/PhysRevLett.79.5218
55. J.F. Liang, J.R. Beene, A.L. Caraley et al., Dynamic polarization in the Coulomb breakup of loosely bound ^{17}F. Phys. Lett. B **681**, 22 (2009). https://doi.org/10.1016/j.physletb.2009.09.055
56. K.E. Rehm, H. Esbensen, C.L. Jiang et al., Fusion cross sections for the proton drip line nucleus ^{17}F at energies below the Coulomb barrier. Phys. Rev. Lett. **81**, 3341 (1998). https://doi.org/10.1103/PhysRevLett.81.3341
57. B.W. Asher, S. Almaraz-Calderon, V. Tripathi et al., Experimental study of the ^{17}F+^{12}C fusion reaction and its implications for fusion of proton-halo systems. Phys. Rev. C **103**, 044615 (2021). https://doi.org/10.1103/PhysRevC.103.044615
58. B.W. Asher, S. Almaraz-Calderon, L.T. Baby et al., The encore active target detector: a multi-sampling ionization chamber. Nucl. Instrum. Methods Phys. Res. Sect. A **1014**, 165724 (2021). https://doi.org/10.1016/j.nima.2021.165724
59. L. Yang, C.J. Lin, H. Yamaguchi et al., Breakup of the proton halo nucleus ^{8}B near barrier energies. Nat. Commun. **13**, 7193 (2022). https://doi.org/10.1038/s41467-022-34767-8
60. L. Yang, C.J. Lin, H. Yamaguchi et al., Insight into the reaction dynamics of proton drip-line nuclear system ^{17}F+^{58}Ni at near-barrier energies. Phys. Lett. B **813**, 136045 (2021). https://doi.org/10.1016/j.physletb.2020.136045
61. Y.J. Yao, C.J. Lin, L. Yang et al., Relative probabilities of breakup channels in reactions of ^{6,7}Li with ^{209}Bi at energies around and above the Coulomb barrier. Chin. Phys. C **45**, 054104 (2021). https://doi.org/10.1088/1674-1137/abe3ee
62. N.R. Ma, L. Yang, C.J. Lin et al., MITA: a multilayer ionization-chamber telescope array for low-energy reactions with exotic nuclei. Eur. Phys. J. A **55**, 87 (2019). https://doi.org/10.1140/epja/i2019-12765-7
63. D.X. Wang, C.J. Lin, L. Yang et al., Compact 16-channel integrated charge-sensitive preamplifier module for silicon strip detectors. Nucl. Sci. Tech. **31**, 48 (2020). https://doi.org/10.1007/s41365-020-00755-0
64. Y. Yanagisawa, S. Kubono, T. Teranishi et al., Low-energy radioisotope beam separator CRIB. Nucl. Instrum. Methods Phys. Res. A **539**, 74 (2005). https://doi.org/10.1016/j.nima.2004.09.041
65. M. Ichimura, N. Austern, C.M. Vincent, Equivalence of post and prior sum rules for inclusive breakup reactions. Phys. Rev. C **32**, 431 (1985). https://doi.org/10.1103/PhysRevC.32.431
66. E.C. Simpson, K.J. Cook, D.H. Luong et al., Disintegration locations in ^{7}Li→^{8}Be transfer-triggered breakup at near-barrier energies. Phys. Rev. C **93**, 024605 (2016). https://doi.org/10.1103/PhysRevC.93.024605
67. M. Mazzocco, C. Signorini, D. Pierroutsakou et al., Reaction dynamics for the system ^{17}F+^{58}Ni at near-barrier energies. Phys. Rev. C **82**, 054604 (2010). https://doi.org/10.1103/PhysRevC.82.054604
68. E. Strano, D. Torresi, M. Mazzocco et al., ^{17}O+^{58}Ni scattering and reaction dynamics around the Coulomb barrier. Phys. Rev. C **94**, 024622 (2016). https://doi.org/10.1103/PhysRevC.94.024622
69. N. Keeley, J.A. Christley, N.M. Clarke et al., The threshold anomaly in the ^{16}O+^{58,60,62,64}Ni systems. Nucl. Phys. A **582**, 314 (1995). https://doi.org/10.1016/0375-9474(94)00485-6
70. N. Keeley, J.S. Lilley, J.X. Wei et al., Fusion excitation function measurements for the ^{16}O+^{58}Ni and ^{16}O+^{62}Ni systems. Nucl. Phys. A **628**, 1 (1998). https://doi.org/10.1016/S0375-9474(97)00597-6
71. L.F. Canto, P.R.S. Gomes, J. Lubian et al., Disentangling static and dynamic effects of low breakup threshold in fusion reactions. J. Phys. G: Nucl. Part. Phys. **36**, 015109 (2009). https://doi.org/10.1088/0954-3899/36/1/015109